Available online at www.sciencedirect.com
ScienceDirect
Journal of Computational Physics 225 (2007) 263–283
JOURNAL OF COMPUTATIONAL PHYSICS
www.elsevier.com/locate/jcp

A computational strategy for the regularized 13 moment equations with enhanced wall-boundary conditions

X.J. Gu *, D.R. Emerson [1]

Computational Science and Engineering Department, CCLRC Daresbury Laboratory, Warrington WA4 4AD, UK

Received 19 April 2006; received in revised form 6 September 2006; accepted 29 November 2006
Available online 19 January 2007

Abstract

The challenge of modeling low-speed rarefied gas flow in the transition regime is well known. In this paper, we propose a numerical solution procedure for the regularized 13 moment equations within a finite-volume framework. The stress and heat flux equations arising in the method of moments are transformed into the governing equations for the stress and heat flux deviators based on their first-order approximation. To model confined flows, a complete set of wall boundary conditions for the 13 moment equations are derived based on the Maxwell wall-boundary model. This has been achieved by expanding the molecular distribution function to fourth-order accuracy in Hermite polynomials. Empirical correction factors are introduced into the boundary conditions and calibrated against direct simulation Monte Carlo data. The numerical predictions obtained from the regularized 13 moment equations and the Navier–Stokes–Fourier equations are compared with data generated using the direct simulation Monte Carlo method for planar Couette flow. For a range of wall velocities and Knudsen numbers (0.012–1.0), the results indicate that the regularized 13 moment equations are in good qualitative agreement with the direct simulation Monte Carlo data. The results also highlight limitations that are caused by the use of a first-order expansion of the third moment.

PACS: 65P40; 65P20; 76AAxx

Keywords: Wall boundary conditions; Rarefied gas dynamics; Microfluidics; Finite volume method; Method of moments; Couette flow; Velocity slip; Temperature jump

1. Introduction

The degree of rarefaction of a gas is generally expressed through the Knudsen number ($Kn = \lambda/L$) which is the ratio of the molecular mean free path, λ, to a typical dimension of the flow field, L. The Boltzmann equation [1] provides an accurate description of a dilute gas at all degrees of rarefaction and describes its state

* Corresponding author. Tel.: +44 1925 603 663; fax: +44 1925 603 634.
E-mail addresses: x.j.gu@dl.ac.uk (X.J. Gu), d.r.emerson@dl.ac.uk (D.R. Emerson).
[1] Tel.: +44 1925 603 221; fax: +44 1925 603 634.

0021-9991/$ - see front matter
doi:10.1016/j.jcp.2006.11.032

through a molecular distribution function that treats the gas as a large number of interacting molecules, colliding and rebounding according to prescribed laws. Solutions of the Boltzmann equation, either directly [2] or through the direct simulation Monte Carlo (DSMC) method [3], entail significant mathematical complexity and can be computationally expensive, particularly for low-speed, low Knudsen number flows in the slip ($Kn < 0.1$) and transition ($0.1 \leqslant Kn < 10$) regimes. These flows are often found in micro-electro-mechanical-systems (MEMS) [4,5].

Due to the difficulties associated with solving the Boltzmann equation, there is significant effort being made to construct alternative solution strategies that can provide an accurate description of a gas with Knudsen numbers that extend into the transition regime. For designing components in MEMS, it is desirable that any new developments have: (i) computational efficiency comparable to conventional hydrodynamic formulations; (ii) the ability to handle real geometries, and (iii) under appropriate conditions, will recover the Navier–Stokes–Fourier solution. The two main approaches used to derive these *extended hydrodynamic* (EHD) equations are the Chapman–Enskog expansion [6] and the method of moments developed by Grad [7].

The Chapman–Enskog approach expands the molecular distribution function in powers of Kn to construct the constitutive relationships. The zeroth-order expansion yields the Euler equations and the first-order results in the Navier–Stokes equations. Higher order expansions yield the Burnett equations (second-order), Super-Burnett equations (third-order), and so on. It is expected that the higher the expansion order is, the resulting set of equations will provide an improved description of any departures from the equilibrium state. However, Grad [8] argued that no matter how high the expansion order is, the resulting system will only describe flows that are already close to the continuum solution. Furthermore, the higher-order equations become linearly unstable and are not suitable for numerical simulation of processes involving small wavelengths [9]. Several researchers [10,11] have presented augmented forms of the second-order constitutive relationship to stabilize the Burnett equations.

In Grad's approach [7], a governing set of partial differential equations representing the moments of the molecular distribution function are derived from the Boltzmann equation. However, moments of higher order always appear in each moment equation and the set of moment equations is not closed. To avoid the necessity of dealing with an infinite number of moment equations, a closure procedure is required that relates the higher-order moments to those of lower order. In the seminal work of Grad [7], the set of moment equations was closed at the second-moment level, which involves 13 moments: density, momentum, energy, heat flux, and pressure deviator. It is interesting to point out that the constitutive relationships established by the Chapman–Enskog method, at any order, can be regarded as a first moment closure method with 5 moments [3]. To close the set of moment equations at the second-moment level, Grad [7] expanded the distribution function in Hermite polynomials about the local Maxwellian to third-order accuracy and set the trace-free part of the third moments to zero. As a result, the original set of 13 moment equations derived by Grad (G13) is hyperbolic and lacks any gradient transport mechanism. They are not suitable for computing boundary layers or predicting shock structures above a Mach number of 1.65 [12].

Recently, Struchtrup and Torrilhon [13] regularized Grad's 13 moment equations (R13) by applying a Chapman–Enskog like expansion to the governing equations of the moments higher than second order. Algebraic constitutive relationships were then established between the higher moments and the second and lower moments. This important procedure introduces gradient transport terms into the second moment equations and changes their character from hyperbolic to parabolic. Subsequently, Struchtrup [14,15] used an order-of-magnitude approach to achieve a similar closure. In contrast, Jin and Slemrod [16] used a visco-elastic regularization procedure to develop a relaxed Burnett system through a relaxation of the pressure deviator and the heat flux. This approach leads to a stable set of 13 governing equations that are weakly parabolic and a detailed comparison between the R13 equations and Jin and Slemrod's regularization has been given by Struchtrup [17]. The shock structures computed with Struchtrup and Torrilhon's closure are smooth and in quantitative agreement with DSMC simulations for Mach numbers up to 3.0 [17,18]. However, to apply this set of moment equations to confined flows, such as those found in microfluidic channels, wall boundary conditions are required. No complete set of wall boundary conditions for the 13 moment equations have appeared in the literature, and this hampers the application of the moment method in MEMS and other confined rarefied gas flows.

To construct wall boundary conditions for the governing moment equations, a scattering kernel is needed that describes the gas–surface interaction [19]. This paper presents a complete set of wall boundary conditions for the 13 moment equations that have been derived using the Maxwell wall-boundary model [20] and expanding the distribution function in Hermite polynomials to fourth-order accuracy. As only a finite number of moments are involved in the approximated molecular distribution function, empirical correction factors are required that will account for any Knudsen layer effects [1]. The values of the empirical correction factors are determined from a set of *numerical experiments* obtained from DSMC studies of planar Couette flow which, although geometrically simple, exhibits all the essential rarefaction effects as the Knudsen number increases. The DSMC data obtained in the present study cover a range of Knudsen numbers and wall velocities and has been used to calibrate and validate the new wall boundary conditions. Moreover, the computed values of the moments are compared with those obtained from the DSMC simulations and the validity of the proposed closure is discussed.

To numerically solve the 13 moment equations for parabolic and elliptic flows within a conventional CFD approach, such as the finite volume (FV) method, is quite challenging because the gradient transport mechanisms are not explicitly expressed in the momentum and energy equations of the moment system. The inadequacy of the standard FV method for the governing equations without any gradient transport terms is well recognized [21], so that methods for dealing with hyperbolic problems are required, such as Riemann solvers [22], TVD schemes [23] and ENO schemes [24] for capturing discontinuities. For high speed flows, Jin et al. [25] developed a one-dimensional non-oscillatory numerical scheme and successfully predicted shock structures up to Mach 10 with the relaxed Burnett system [16]. These schemes are complex and computationally expensive for multidimensional confined flow, particularly at low speed. This paper proposes a solution strategy for the R13 equations which is able to employ conventional FV techniques associated with elliptic flow problems. In our approach, the stress and heat flux equations in the R13 system are transformed into the governing equations for the stress and heat flux deviators from their first-order approximations, respectively. They can then be solved numerically by coupling with the momentum and energy equations.

In Section 2, Grad's method of moments and Struchtrup and Torrilhon's second-moment closure are briefly described. In the subsequent section, the molecular phase-density distribution function is expanded in Hermite polynomials to fourth-order accuracy about an equilibrium distribution. A complete set of wall boundary conditions for the 13 moment equations are presented in Section 4 based on this polynomial expansion and Maxwell's wall-boundary model. In Section 5, the numerical strategy is discussed and results obtained from the NSF and R13 equations for planar Couette flow, covering a range of Knudsen numbers, are presented in Section 6 and compared with DSMC data.

2. Method of moments and second-moment closure

Kinetic theory accounts for a molecule's movement and interaction through a molecular phase-density distribution function, $F(\boldsymbol{\xi}, \boldsymbol{x}, t)$, which satisfies the Boltzmann integro-differential equation [1], where $\boldsymbol{x}$ and $\boldsymbol{\xi}$ are the position and velocity vectors, respectively, of a molecule at time t, and $F(\boldsymbol{\xi}, \boldsymbol{x}, t)\,\mathrm{d}\boldsymbol{x}\,\mathrm{d}\boldsymbol{\xi}$ gives the number of molecules whose velocities lie within $\mathrm{d}\boldsymbol{\xi}$ in a volume element $\mathrm{d}\boldsymbol{x}$. For convenience, a mass distribution function is used in the present study and is defined by

$$f(\boldsymbol{\xi}, \boldsymbol{x}, t) = mF(\boldsymbol{\xi}, \boldsymbol{x}, t), \tag{1}$$

where m is the mass of a molecule. Once the distribution function, f, is known, its moments with respect to $\boldsymbol{\xi}$ can be determined. For example, the density, ρ, and the momentum, ρu_i, can be obtained from

$$\rho = \int f \,\mathrm{d}\boldsymbol{\xi} \quad \text{and} \quad \rho u_i = \int \xi_i f \,\mathrm{d}\boldsymbol{\xi}, \tag{2}$$

where ξ_i represents the particle velocity. An intrinsic or peculiar velocity is introduced as

$$c_i = \xi_i - u_i \tag{3}$$

so that the moments with respect to u_i can be conveniently calculated.

In the method of moments, a set of N moments are used to describe the state of the gas through

$$\rho_{i_1 i_2 \ldots\ldots i_N} = \int c_{i_1} c_{i_2} \ldots\ldots c_{i_N} f \, \mathrm{d}\boldsymbol{\xi}. \tag{4}$$

The first 13 moments chosen by Grad in the second-moment closure are $\boldsymbol{\psi} = (1, \xi_i, c^2, c_i c_j, c^2 c_i/2)$, where $c^2 = c_k c_k$, and the thermal energy, pressure tensor, and heat flux are given by $\rho\varepsilon$, p_{ij}, and q_i, respectively. Any moment can be expressed by its trace and traceless part [13–15]. For example, the pressure tensor can be separated as follows:

$$p_{ij} = p\delta_{ij} + p_{\langle ij \rangle} = p\delta_{ij} + \sigma_{ij} = \int c_i c_j f \, \mathrm{d}\boldsymbol{\xi}, \tag{5}$$

where δ_{ij} is the Kronecker delta function, $p = p_{kk}/3$ is the pressure, and $\sigma_{ij} = p_{\langle ij \rangle}$ is the deviatoric stress tensor. The angular brackets denote the traceless part of a symmetric tensor. Furthermore, the thermal energy density is given by

$$\rho\varepsilon = \frac{3}{2}\rho\frac{k}{m}T = \frac{1}{2}\int c^2 f \, \mathrm{d}\boldsymbol{\xi}. \tag{6}$$

The temperature, T, is related to the pressure and density by the ideal gas law, $p = \rho(k/m)T = \rho RT$, where k is Boltzmann's constant and R is the gas constant. The heat flux vector is

$$q_i = \frac{1}{2}\int c^2 c_i f \, \mathrm{d}\boldsymbol{\xi}. \tag{7}$$

Multiplying Boltzmann's equation by $\boldsymbol{\psi}$ and integrating over velocity space for Maxwellian molecules yields the 13 moment equations [13]:

$$\frac{\partial \rho}{\partial t} + \frac{\partial \rho u_k}{\partial x_k} = 0, \tag{8}$$

$$\frac{\partial \rho u_i}{\partial t} + \frac{\partial \rho u_i u_k}{\partial x_k} + \frac{\partial \sigma_{ik}}{\partial x_k} = -\frac{\partial p}{\partial x_i}, \tag{9}$$

$$\frac{3}{2}R\frac{\partial \rho T}{\partial t} + \frac{3}{2}R\frac{\partial \rho T u_k}{\partial x_k} + \frac{\partial q_k}{\partial x_k} = -p\frac{\partial u_k}{\partial x_k} - \sigma_{ik}\frac{\partial u_i}{\partial x_k}, \tag{10}$$

$$\frac{\partial \sigma_{ij}}{\partial t} + \frac{\partial \sigma_{ij} u_k}{\partial x_k} + \frac{\partial m_{ijk}}{\partial x_k} = -\frac{p}{\mu}\sigma_{ij} - 2p\frac{\partial u_{\langle i}}{\partial x_{j\rangle}} - 2\sigma_{k\langle i}\frac{\partial u_{j\rangle}}{\partial x_k} - \frac{4}{5}\frac{\partial q_{\langle i}}{\partial x_{j\rangle}}, \tag{11}$$

$$\begin{aligned}\frac{\partial q_i}{\partial t} + \frac{\partial q_i u_k}{\partial x_k} + \frac{1}{2}\frac{\partial R_{ik}}{\partial x_k} = {} & -\frac{2}{3}\frac{p}{\mu}q_i - \frac{5}{2}pR\frac{\partial T}{\partial x_i} - \frac{7}{2}\sigma_{ik}R\frac{\partial T}{\partial x_k} - RT\frac{\partial \sigma_{ik}}{\partial x_k} + \frac{\sigma_{ik}}{\rho}\frac{\partial p}{\partial x_k} + \frac{\sigma_{ij}}{\rho}\frac{\partial \sigma_{jk}}{\partial x_k} \\ & - \frac{7}{5}q_k\frac{\partial u_i}{\partial x_k} - \frac{2}{5}q_k\frac{\partial u_k}{\partial x_i} - \frac{2}{5}q_i\frac{\partial u_k}{\partial x_k} - \frac{1}{6}\frac{\partial \Delta}{\partial x_i} - m_{ijk}\frac{\partial u_j}{\partial x_k},\end{aligned} \tag{12}$$

where μ is the viscosity. Eqs. (8)–(10) are the conservation laws for mass, momentum, and energy, where the values of σ_{ij} and q_i are determined from their governing equations. However, m_{ijk}, R_{ij}, and Δ, appearing in Eqs. (11) and (12), are unknowns and correspond to

$$m_{ijk} = \rho_{\langle ijk \rangle}, \quad R_{ij} = \rho_{\langle ij \rangle rr} - 7RT\sigma_{ij}, \quad \text{and} \quad \Delta = \rho_{rrss} - 15pRT. \tag{13}$$

Closure procedures are therefore required to build constitutive models for the terms appearing in Eq. (13) and the approaches followed by Grad [7] and Struchtrup and Torrilhon [13] will be briefly described.

2.1. Grad's closure: G13 moment equations

Grad [7] expanded the distribution function, f, in Hermite polynomials about the local equilibrium Maxwellian. The third-order approximation of the distribution function, $f^{(3)}$, was used by Grad to close the set of moment equations at the second moment level i.e.

$$f^{(3)} = f_{\mathrm{M}}\left\{1 + \frac{1}{2}\frac{\sigma_{ij}}{pRT}c_i c_j - \frac{1}{pRT}c_i q_i\left(1 - \frac{c^2}{5RT}\right) + \frac{m_{ijk}}{6p(RT)^2}c_i c_j c_k\right\}, \tag{14}$$

where f_M is the local Maxwellian distribution function given by

$$f_M = \frac{\rho}{\sqrt{(2\pi RT)^3}} \exp\left(-\frac{c^2}{2RT}\right). \tag{15}$$

In Grad's original closure procedure, the term m_{ijk} appeared in the molecular phase-density function. This was resolved by setting the term to zero and Eq. (14) becomes the Grad distribution function:

$$f_G = f_M\left\{1 + \frac{1}{2}\frac{\sigma_{ij}}{pRT}c_i c_j - \frac{1}{pRT}c_i q_i\left(1 - \frac{c^2}{5RT}\right)\right\}, \tag{16}$$

which results in the additional terms appearing in Eq. (13), R_{ij} and Δ, also being equal to zero.

2.2. Struchtrup and Torrilhon's closure: R13 moment equations

Instead of using the molecular distribution function to calculate m_{ijk}, R_{ij}, and Δ, Struchtrup and Torrilhon [13] applied a Chapman–Enskog-like expansion to the governing equations of the higher moments with linearized production terms for Maxwell molecules. The zeroth-order approximation, given by $m_{ijk}^{(0)} = R_{ij}^{(0)} = \Delta^{(0)} = 0$, corresponds to Grad's original closure and a first-order approximation was therefore used to correct the G13 moment equations. Subsequently, Struchtrup [14,15] used an order-of-magnitude approach to achieve similar approximations that included the nonlinear components in the production terms:

$$m_{ijk} = -\frac{2\mu}{p}\left(RT\frac{\partial \sigma_{\langle ij}}{\partial x_{k\rangle}} + \frac{4}{5}q_{\langle i}\frac{\partial u_j}{\partial x_{k\rangle}} + R\sigma_{\langle ij}\frac{\partial T}{\partial x_{k\rangle}} - \frac{\sigma_{\langle ij}}{\rho}\frac{\partial p}{\partial x_{k\rangle}}\right), \tag{17}$$

$$R_{ij} = -\frac{24}{5}\frac{\mu}{p}\left\{RT\frac{\partial q_{\langle i}}{\partial x_{j\rangle}} + 2Rq_{\langle i}\frac{\partial T}{\partial x_{j\rangle}} - \frac{q_{\langle i}}{\rho}\frac{\partial p}{\partial x_{j\rangle}} + \frac{5}{7}RT\left(\sigma_{k\langle i}\frac{\partial u_{j\rangle}}{\partial x_k} + \sigma_{k\langle i}\frac{\partial u_k}{\partial x_{j\rangle}} - \frac{2}{3}\sigma_{ij}\frac{\partial u_k}{\partial x_k}\right)\right\} - \frac{4}{7}\frac{1}{\rho}\sigma_{k\langle i}\sigma_{j\rangle k}, \tag{18}$$

$$\Delta = -12\frac{\mu}{p}\left\{\frac{7}{2}Rq_k\frac{\partial T}{\partial x_k} - \frac{q_k}{\rho}\frac{\partial p}{\partial x_k} + RT\left(\frac{\partial q_k}{\partial x_k} + \sigma_{ij}\frac{\partial u_i}{\partial x_j}\right)\right\} - \frac{\sigma_{ij}\sigma_{ij}}{\rho}, \tag{19}$$

and these are used to close the set of Eqs. (8)–(12) in the present study. The linear parts of Eqs. (17) and (18) are given by

$$m_{ijk}^L = -\frac{2\mu}{\rho}\frac{\partial \sigma_{\langle ij}}{\partial x_{k\rangle}} \quad \text{and} \quad R_{ij}^L = -\frac{24}{5}\frac{\mu}{\rho}\frac{\partial q_{\langle i}}{\partial x_{j\rangle}}. \tag{20}$$

The terms contained in Eq. (20) were neglected in Grad's original closure but are important because they provide the gradient transport mechanism for σ_{ij} and q_i and help to stabilize the 13 moment equations.

3. The fourth-order approximation

The governing equations for the moments of f describe the relationship between the macroscopic quantities of the flow. However, they do not give details of f itself explicitly but this can be constructed from the values of its moments as an approximation to the solution of the Boltzmann equation. Grad expanded f in Hermite polynomials as

$$f = f_M\sum_{n=0}^{\infty}\frac{1}{n!}a_A^{(n)}H_A^{(n)} = f_M\left(a^{(0)}H^{(0)} + a_i^{(1)}H_i^{(1)} + \frac{1}{2!}a_{ij}^{(2)}H_{ij}^{(2)} + \frac{1}{3!}a_{ijk}^{(3)}H_{ijk}^{(3)} + \ldots.\right), \tag{21}$$

where $H_A^{(n)}$ are the Hermite functions and $a_A^{(n)}$ the coefficients. All of the polynomial coefficients are linear combinations of the moments of f. To accurately describe the state of a gas an infinite number of moments is required to reconstruct the distribution function. However, for gases not too far from equilibrium, a finite number of moments should provide an adequate approximation. The first five polynomials and their

coefficients are given in Appendix. Eq. (16) represents the incomplete third-order approximation to f in Hermite polynomials, as used by Grad [7], to close the system at the second moment level.

The nonequilibrium effects become stronger as the flow approaches the solid wall. If a higher-order approximation for f were employed near the solid surface, it is anticipated that it would provide an improved description of the near-wall flow. The complete third-order approximation to f, given by Eq. (14), is one option that can be used to study the flow in the proximity of the wall. In the present study, the distribution function has been expanded in Hermite polynomials to fourth-order, $f^{(4)}$, and then used to obtain the wall boundary conditions for the moment equations. Making use of Hermite functions and their coefficients, as listed in Appendix, the expression can be written as

$$f^{(4)} = f_{\mathrm{M}}\left[1 + \frac{\sigma_{ij}}{2pRT}c_i c_j - \frac{1}{pRT}c_i q_i\left(1 - \frac{c^2}{5RT}\right) + \frac{m_{ijk}}{6p(RT)^2}c_i c_j c_k + \frac{\phi_{ijkl}}{24p(RT)^3}c_i c_j c_k c_l + \left(\frac{c^2}{7RT} - 1\right)\frac{R_{ij}c_i c_j}{4p(RT)^2} - \frac{c^2\Delta}{12p(RT)^2} + \frac{c^4\Delta}{120p(RT)^3} + \frac{\Delta}{8pRT}\right], \tag{22}$$

where, $\phi_{ijkl} = \rho_{\langle ijkl\rangle}$, represents the fourth moment. Its first-order approximation is given by [15]

$$\phi_{ijkl} = -\frac{12}{7\mathscr{C}_{00}^{(4)}}\frac{\mu}{p}\left(R_{\langle ij} + 7RT\sigma_{\langle ij}\right)\frac{\partial u_k}{\partial x_{l\rangle}} - \frac{\mathscr{Y}_{0,00}^{4,0,2}}{\mathscr{C}_{00}^{(4)}}\frac{\sigma_{\langle ij}\sigma_{kl\rangle}}{\rho}. \tag{23}$$

In Eq. (23), $\mathscr{C}_{00}^{(4)}$ and $\mathscr{Y}_{0,00}^{4,0,2}$ are entries in the collision production matrices $\mathscr{C}_{ab}^{(n)}$ and $\mathscr{Y}_{a,bc}^{n,r,m}$ for the fourth moment and have values of 1.8731 and −0.3806, respectively, for Maxwell molecules [26].

4. Boundary conditions at the wall

One of the difficulties encountered in any investigation of wall boundary conditions is due to a limited understanding of the structure of surface layers of solid bodies and of the effective interaction potential of the gas molecules with the wall. A scattering kernel represents a fundamental concept in gas–surface interactions, by means of which other quantities should be defined [19]. At present, there is no complete set of wall boundary conditions available in the literature for the 13 moment equations. Maxwell's boundary condition [20] is one of the simplest models and it states that a fraction, $(1-\alpha)$, of gas molecules will undergo *specular* reflection while the remaining fraction, α, will be *diffusely* reflected with a Maxwellian distribution, f_{M}^{w}, at the temperature of the wall, T_{w}. In a frame where the coordinates, (x_1, x_2, x_3), are attached to the wall, with x_2 normal to the wall, such that all molecules with $\xi_2 < 0$ are incident upon the wall and molecules with $\xi_2 \geqslant 0$ are emitted by the wall, Maxwell's boundary condition can be expressed by [27]

$$f^{w}(\xi_1,\xi_2,\xi_3) = \begin{cases} \alpha f_{\mathrm{M}}^{w} + (1-\alpha)f(\xi_1,-\xi_2,\xi_3), & \xi_2 \geqslant 0 \\ f(\xi_1,\xi_2,\xi_3), & \xi_2 < 0 \end{cases}, \tag{24}$$

and

$$f_{\mathrm{M}}^{w}(\xi_1,\xi_2,\xi_3) = \frac{\rho_{\mathrm{w}}}{\sqrt{(2\pi RT_{\mathrm{w}})^3}}\exp\left(-\frac{\xi_1^2+\xi_2^2+\xi_3^2}{2RT_{\mathrm{w}}}\right). \tag{25}$$

In Eq. (25), ρ_{w} is the density of the thermalized particles and needs to be determined to ensure that no particles accumulate on the wall. By definition, the value of any moment at the wall can be obtained from

$$\int c_{i_1}c_{i_2}\ldots c_{i_n}f(\xi_1,\xi_2,\xi_3)\,\mathrm{d}\boldsymbol{\xi} = \int c_{i_1}c_{i_2}\ldots c_{i_n}f^{w}(\xi_1,\xi_2,\xi_3)\,\mathrm{d}\boldsymbol{\xi} \tag{26}$$

Using Eq. (24), Eq. (26) becomes

$$\int_{\xi_2\geqslant 0} c_{i_1}c_{i_2}\ldots c_{i_n}f(\xi_1,\xi_2,\xi_3)\,\mathrm{d}\boldsymbol{\xi} = \int_{\xi_2\geqslant 0} c_{i_1}c_{i_2}\ldots c_{i_n}[\alpha f_{\mathrm{M}}^{w} + (1-\alpha)f(\xi_1,-\xi_2,\xi_3)]\,\mathrm{d}\boldsymbol{\xi} \tag{27}$$

Since there is no gas flow through the wall, $c_2 = \xi_2$. For ease of presentation, the wall boundary conditions for 2D planar flow, $x_1 - x_2$, are presented below. The extension to 3D is straightforward. However, not all of the moments are restricted by Eq. (24) if f is approximated by a finite number of its moments [7]. Grad considered the special case of $\alpha = 0$ and concluded that only moments that are odd functions of ξ_2 can be used to construct the wall boundary conditions. This limits the choice of moments to $\boldsymbol{\psi} = (c_2\ c_1c_2\ c^2c_2\ c_1c_1c_2\ c^2c_2c_2c_2\ c_1c_2c_2c_2\ c^2c_1c_2\ c^4c_2)$. Replacing f in Eq. (27) with its fourth-order approximation, $f^{(4)}$, gives the following set of wall boundary conditions:

$$\rho_w\sqrt{RT_w} = \frac{p_\alpha}{\sqrt{RT}}, \tag{28}$$

$$u_{1s} = -\frac{2-\alpha}{\alpha}\beta_u\sqrt{\frac{\pi RT}{2}}\frac{\sigma_{12}}{p_\alpha} - \frac{m_{122}}{2p_\alpha} - \frac{q_1}{5p_\alpha}, \tag{29}$$

$$RT - RT_w = -\frac{2-\alpha}{\alpha}\beta_T\sqrt{\frac{\pi RT}{2}}\frac{q_2}{2p_\alpha} - \frac{RT\sigma_{22}}{4p_\alpha} + \frac{u_{1s}^2}{4} + \frac{35\phi_{2222} - 75R_{22} - 28\Delta}{840p_\alpha}, \tag{30}$$

$$\sigma_{11} = -\frac{2-\alpha}{\alpha}\beta_{\sigma_{11}}\sqrt{\frac{\pi RT}{2}}\frac{5m_{112} + 2q_2}{5RT} + p_\alpha\left(\frac{u_{1s}^2}{RT} + \frac{T_w}{T} - 1\right) - \frac{105\phi_{1122} + 15(R_{11} + R_{22}) + 7\Delta}{210RT}, \tag{31}$$

$$\sigma_{22} = -\frac{2-\alpha}{\alpha}\beta_{\sigma_{22}}\sqrt{\frac{\pi RT}{2}}\frac{(105m_{222} + 196q_2)}{210RT} - \frac{105\phi_{2222} + 195R_{22} + 56\Delta}{630RT} + \frac{2}{3}p_\alpha\left[\left(\frac{T_w}{T}\right)^2 - 1\right] + \frac{p_\alpha u_{1s}^2}{9RT}\frac{T_w}{T}, \tag{32}$$

$$\sigma_{12} = -\frac{\alpha}{2-\alpha}\beta_{\sigma_{12}}\sqrt{\frac{2}{\pi RT}}\left(\frac{2}{3}\frac{T_w}{T}u_{1s}p_\alpha + m_{122} + \frac{2}{5}q_1\right) - \frac{3R_{12} + 7\phi_{2212}}{21RT}, \tag{33}$$

$$q_1 = -\frac{5}{18}\frac{2-\alpha}{\alpha}\beta_{q_1}\sqrt{\frac{\pi RT}{2}}\left(7\sigma_{12} + \frac{R_{12}}{RT}\right) - \frac{5}{18}\frac{u_{1s}p_\alpha}{RT}\left(u_{1s}^2 + 6RT_w\right) - \frac{10}{9}m_{122}, \tag{34}$$

and

$$q_2 = -\frac{\alpha}{2-\alpha}\beta_{q_2}\sqrt{\frac{RT}{2\pi}}\left\{\frac{108R_{22} + 63\Delta - 70\phi_{2222}}{294RT} - \frac{p_\alpha u_{1s}^2}{RT}\frac{\left(12RT_w + u_{1s}^2\right)}{14RT} + \frac{12}{7}\left[p + \sigma_{22} - p_\alpha\left(\frac{T_w}{T}\right)^2\right]\right\}, \tag{35}$$

where

$$p_\alpha = p + \frac{\sigma_{22}}{2} - \frac{30R_{22} + 7\Delta}{840RT} - \frac{\phi_{2222}}{24RT}, \tag{36}$$

and u_{1s} is the slip velocity relative to the wall. In the derivation of the above set of wall boundary conditions, Eq. (28) has been used to eliminate ρ_w in Eqs. (29)–(35).

4.1. Calibration of the boundary values

In deriving the boundary conditions, given by Eqs. (29)–(35), the distribution function has been constructed using a finite number of moments. Consequently, the values of some moments at the wall are underestimated and others are overestimated due to the effect of the Knudsen layer [1]. To compensate for this necessary simplification, empirical correction factors, $\beta_\varphi(\varphi = u, T, \sigma_{11}, \sigma_{22}, \sigma_{12}, q_1, q_2)$ have been introduced into the boundary conditions. This type of approach has been used before to correct the slip-velocity and temperature jump for the Navier–Stokes equations [1,27–31].

The values of the coefficients, β_φ, can be determined either from solutions of the Boltzmann equation or from DSMC calculations. The latter approach has been adopted in the present study using planar Couette flow as the test case. Although geometrically simple, it exhibits all the important flow phenomena and can readily be used to find the values of β_φ. The DSMC code developed by Bird [3] has been used for the simulations and was modified to obtain all moments involved in the boundary conditions to enable the values of $\beta_\varphi(\varphi = u, T, \sigma_{11}, \sigma_{22}, \sigma_{12}, q_1, q_2)$ to be determined from Eqs. (29)–(35).

Planar Couette flow represents a classical problem in rarefied gas dynamics and it has often been used to investigate features such as velocity-slip, temperature jump and Knudsen layers [32–34]. In the present study, the coordinates are chosen such that the upper plate moves with velocity u_w in the x_1 direction and x_2 is the direction perpendicular to the plates. The lower plate remains stationary. The variable hard sphere (VHS) model for argon has been employed with the gas constant $R = 208$ J/kg K. Both plates have a fixed wall temperature, $T_w = 273$ K, and values of the wall velocity were 50, 100, 300, 600 and 1000 m/s. The Knudsen number for this problem was defined as $Kn = \lambda/L$, where L is the distance between the two infinite parallel plates and the molecular mean free path is given by

$$\lambda = \frac{\mu}{p}\sqrt{\frac{\pi RT}{2}}. \tag{37}$$

The wall temperature, T_w, and the initial pressure have been used as reference values to estimate λ. Seven Knudsen numbers, ranging from 0.012 to 1.0, were investigated in the DSMC simulations to estimate the values of β_φ. The viscosity was obtained from Sutherland's law [35]

$$\mu = \mu_0\left(\frac{T}{T_0}\right)^{1.5}\frac{T_0 + S}{T + S}, \tag{38}$$

where the reference viscosity and temperature are, $\mu_0 = 21.25 \times 10^{-6}$ Pa s and $T_0 = 273$ K, respectively, and Sutherland's constant, $S = 144$ K, for argon. The accommodation coefficient, α, was assigned a value of unity i.e. fully diffuse reflection has been assumed for both walls.

5. The numerical method

The thirteen moment equations have often been used to study shock structures where the flows are hyperbolic in nature [12,18,25]. In the case of low-speed rarefied gas flow, such as those found in micro-devices, the system is parabolic or elliptic. Using a hyperbolic flow solver to solve elliptic flows is inefficient and expensive. Regularization of Grad's 13 moment equations introduces gradient transport terms into the governing equations for the stress and heat flux. However, the gradient transport mechanisms for momentum and energy are implicitly included in the stress and heat flux terms and are not explicitly expressed in the momentum and energy equations. This imposes great difficulties in solving the set of R13 moment equations numerically with a finite volume (FV) method, particularly for confined and steady-state flows. Since the gradient transport mechanisms of momentum and energy are represented by the first-order approximations of stress and heat flux

$$\sigma_{ik}^{(1)} = -2\mu\frac{\partial u_{\langle i}}{\partial x_{k\rangle}} \quad \text{and} \quad q_k^{(1)} = -\frac{15}{4}R\mu\frac{\partial T}{\partial x_k}, \tag{39}$$

it is possible to define the stress and heat flux deviators as

$$\rho g_{ik} = \sigma_{ik} - \sigma_{ik}^{(1)} \quad \text{and} \quad \rho h_k = q_k - q_k^{(1)}, \tag{40}$$

where g_{ik} and h_k denote the specific stress and heat flux deviators, respectively. Eq. (40) can be inserted into Eqs. (17) and (18) to give

$$m_{ijk} = -\frac{2}{3}\mu\frac{\partial g_{ij}}{\partial x_k} - \frac{2}{3}\mu g_{ij}\frac{\partial \ln\rho}{\partial x_k} - \frac{2\mu}{3\rho}\frac{\partial \sigma_{ij}^{(1)}}{\partial x_k} + n_{ijk}, \tag{41}$$

and

$$R_{ij} = -\frac{12}{5}\mu\frac{\partial h_i}{\partial x_j} - \frac{12}{5}\mu h_i\frac{\partial \ln\rho}{\partial x_j} - \frac{12}{5}\frac{\mu}{\rho}\frac{\partial q_i^{(1)}}{\partial x_j} + S_{ij}, \tag{42}$$

where

$$n_{ijk} = -\frac{2\mu}{3\rho}\left[\left(\frac{\partial\sigma_{ik}}{\partial x_j} + \frac{\partial\sigma_{jk}}{\partial x_i}\right) - \frac{2}{5}\left(\frac{\partial\sigma_{il}}{\partial x_l}\delta_{jk} + \frac{\partial\sigma_{jl}}{\partial x_l}\delta_{ik} + \frac{\partial\sigma_{kl}}{\partial x_l}\delta_{ij}\right)\right] - \frac{2\mu}{p}\left(\frac{4}{5}q_{\langle i}\frac{\partial u_j}{\partial x_{k\rangle}} + R\sigma_{\langle ij}\frac{\partial T}{\partial x_{k\rangle}} - \frac{\sigma_{\langle ij}}{\rho}\frac{\partial p}{\partial x_{k\rangle}}\right) \tag{43}$$

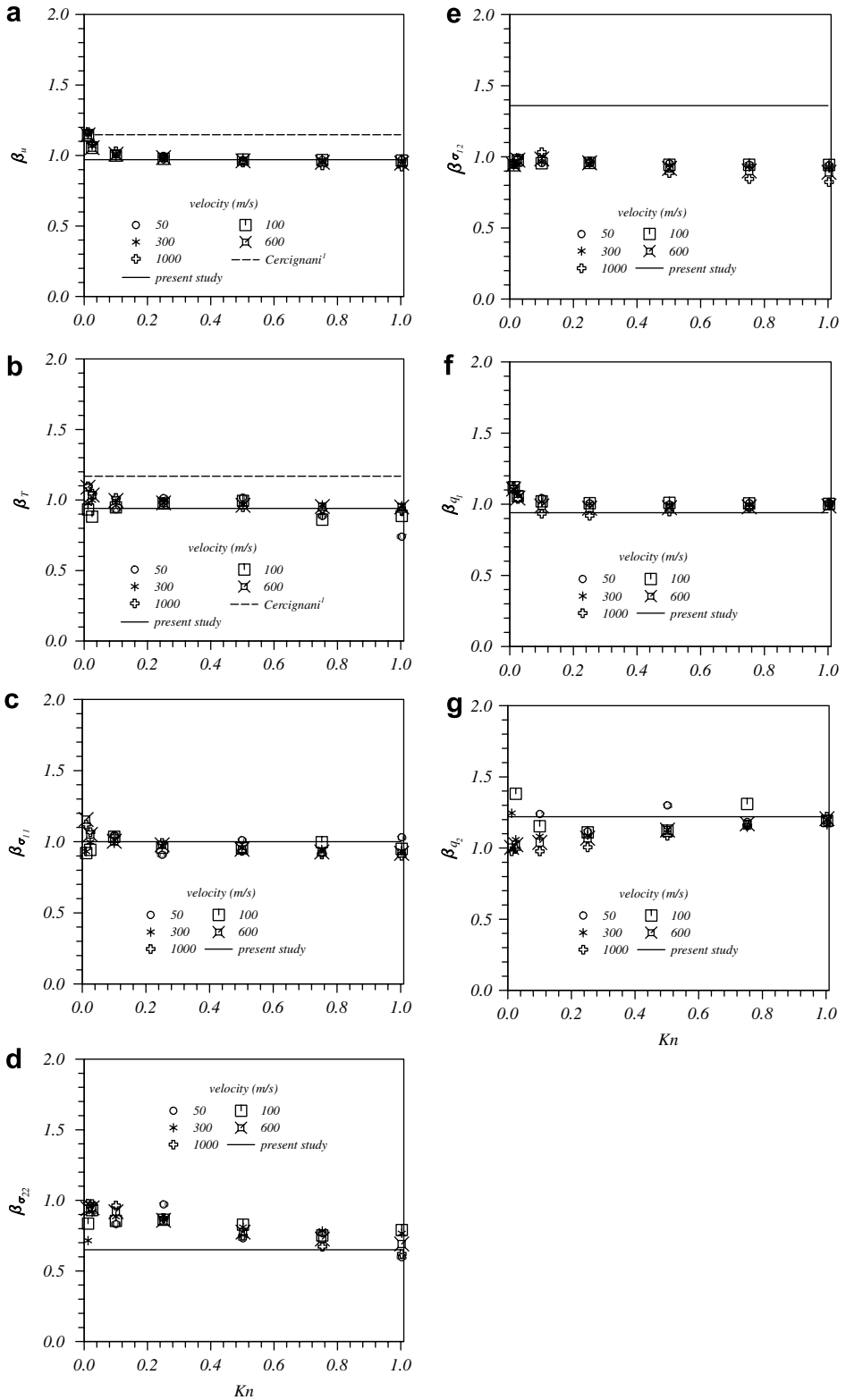

Fig. 1. Determination of the correction factors, β_φ, for the 13 moment wall boundary conditions. Symbols represent values obtained from DSMC calculations of planar Couette flow for five different wall velocities. The solid lines indicate values used in the present study.

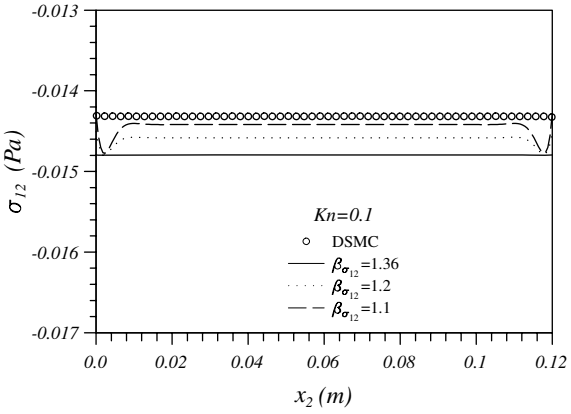

Fig. 2. Determination of optimum $\beta_{\sigma_{12}}$ coefficient through comparison of DSMC data and predicted values of shear stress, σ_{12}, for planar Couette flow with initial conditions $Kn = 0.1$, $T_w = 273$ K and $u_w = 100$ m/s.

Table 1
Correction factors β_φ for wall boundary conditions

φ	u	T	σ_{11}	σ_{22}	σ_{12}	q_1	q_2
β_φ	0.97	0.94	1.0	0.65	1.36	0.94	1.22

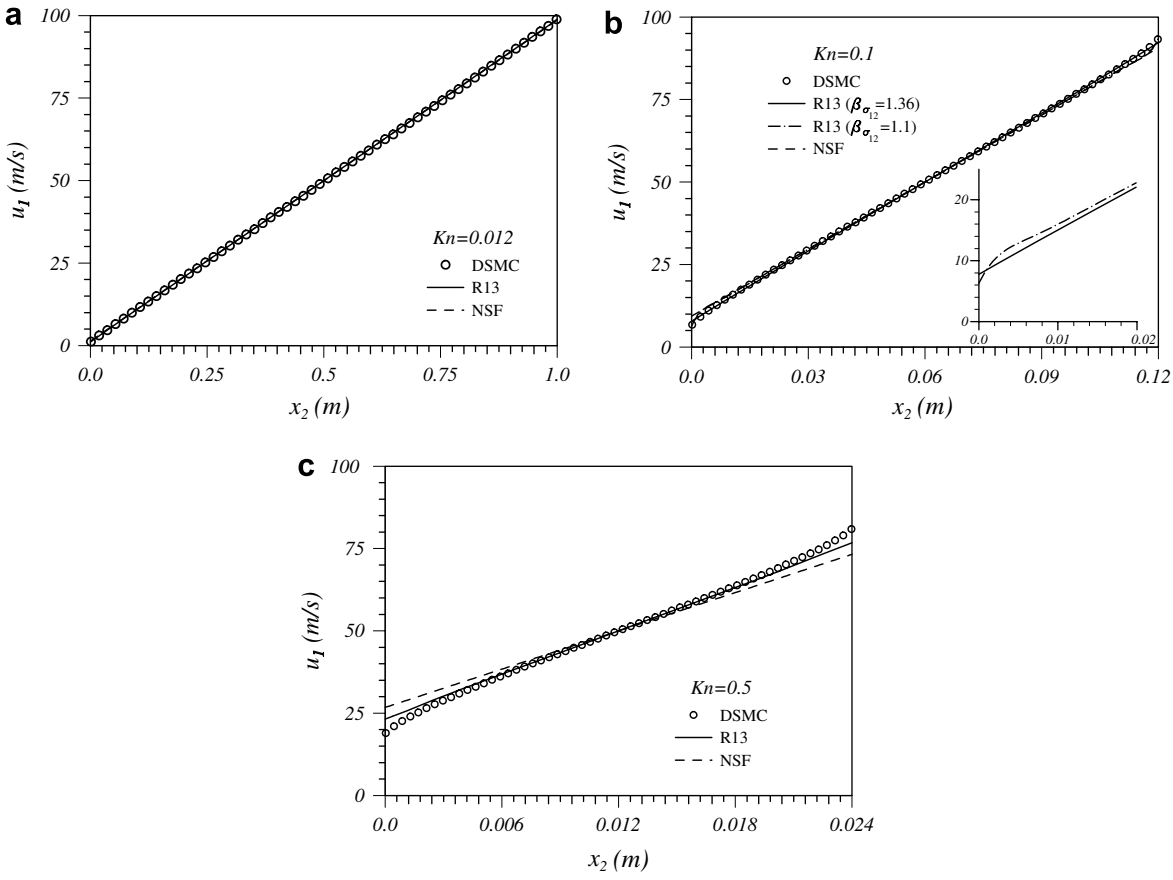

Fig. 3. Predicted velocity profiles at a range of Knudsen numbers with initial conditions: $T_w = 273$ K and $u_w = 100$ m/s.

and

$$S_{ij} = -\frac{12}{5}\frac{\mu}{\rho}\frac{\partial q_j}{\partial x_i} + \frac{8}{5}\frac{\mu}{\rho}\frac{\partial q_k}{\partial x_k}\delta_{ij} - \frac{24}{5}\frac{\mu}{p}\left\{2Rq_{\langle i}\frac{\partial T}{\partial x_{j\rangle}} - \frac{q_{\langle i}}{\rho}\frac{\partial p}{\partial x_{j\rangle}} + \frac{5}{7}RT\left(\sigma_{k\langle i}\frac{\partial u_{j\rangle}}{\partial x_k} + \sigma_{k\langle i}\frac{\partial u_k}{\partial x_{j\rangle}} - \frac{2}{3}\sigma_{ij}\frac{\partial u_k}{\partial x_k}\right)\right\} - \frac{4}{7}\frac{1}{\rho}\sigma_{k\langle i}\sigma_{j\rangle k}. \tag{44}$$

Using Eqs. (39)–(42), it is possible to rewrite Eqs. (9)–(12) in a steady-state form as follows

$$\frac{\partial \rho u_i u_k}{\partial x_k} - \frac{\partial}{\partial x_k}\left(\mu\frac{\partial u_i}{\partial x_k}\right) = -\frac{\partial p}{\partial x_i} + \frac{\partial}{\partial x_k}\left(\mu\frac{\partial u_k}{\partial x_i}\right) - \frac{2}{3}\frac{\partial}{\partial x_i}\left(\mu\frac{\partial u_l}{\partial x_l}\right) - \underline{\frac{\partial \rho g_{ik}}{\partial x_k}}, \tag{45}$$

$$\frac{\partial \rho u_k T}{\partial x_k} - \frac{\partial}{\partial x_k}\left(\frac{5}{2}\mu\frac{\partial T}{\partial x_k}\right) = -\frac{2}{3R}\left(p\frac{\partial u_k}{\partial x_k} + \sigma_{ik}\frac{\partial u_i}{\partial x_k}\right) - \underline{\frac{2}{3R}\frac{\partial \rho h_k}{\partial x_k}}, \tag{46}$$

$$\frac{\partial \rho u_k g_{ij}}{\partial x_k} - \frac{\partial}{\partial x_k}\left(\frac{2}{3}\mu\frac{\partial g_{ij}}{\partial x_k}\right) = -\frac{p}{\mu}\rho g_{ij} - 2\sigma_{k\langle i}\frac{\partial u_{j\rangle}}{\partial x_k} - \frac{4}{5}\frac{\partial q_{\langle i}}{\partial x_{j\rangle}} - \frac{\partial n_{ijk}}{\partial x_k} + \frac{2}{3}\frac{\partial}{\partial x_k}\left(\mu g_{ij}\frac{\partial \ln \rho}{\partial x_k}\right) - \left[\frac{\partial \sigma_{ij}^{(1)} u_k}{\partial x_k} - \frac{2}{3}\frac{\partial}{\partial x_k}\left(\frac{\mu}{\rho}\frac{\partial \sigma_{ij}^{(1)}}{\partial x_k}\right)\right] \tag{47}$$

and

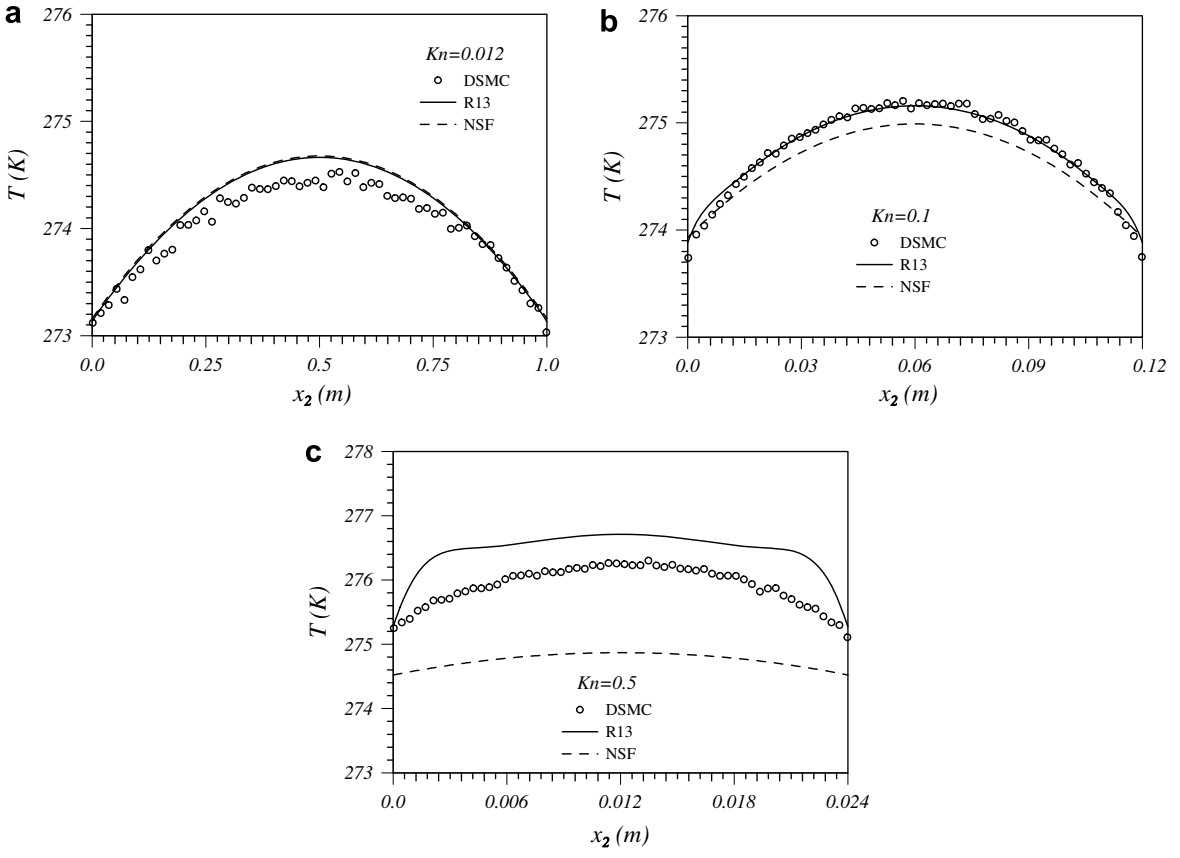

Fig. 4. Predicted temperature profiles at a range of Knudsen numbers with initial conditions: $T_w = 273$ K and $u_w = 100$ m/s.

$$\frac{\partial \rho u_k h_i}{\partial x_k} - \frac{\partial}{\partial x_k}\left(\frac{6}{5}\mu\frac{\partial h_i}{\partial x_k}\right) = -\frac{2}{3}\frac{p}{\mu}\rho h_i - \frac{7}{2}\sigma_{ik}R\frac{\partial T}{\partial x_k} - RT\frac{\partial \sigma_{ik}}{\partial x_k} + \frac{\sigma_{ik}}{\rho}\frac{\partial p}{\partial x_k} + \frac{\sigma_{ij}}{\rho}\frac{\partial \sigma_{jk}}{\partial x_k} - \frac{7}{5}q_k\frac{\partial u_i}{\partial x_k} - \frac{2}{5}q_k\frac{\partial u_k}{\partial x_i} - \frac{2}{5}q_i\frac{\partial u_k}{\partial x_k} - \frac{1}{6}\frac{\partial \Delta}{\partial x_i} - m_{ijk}\frac{\partial u_j}{\partial x_k} - \frac{1}{2}\frac{\partial S_{ik}}{\partial x_k} + \frac{6}{5}\frac{\partial}{\partial x_k}\left(\mu h_i\frac{\partial \ln \rho}{\partial x_k}\right) - \left[\frac{\partial u_k q_i^{(1)}}{\partial x_k} - \frac{6}{5}\frac{\partial}{\partial x_k}\left(\frac{\mu}{\rho}\frac{\partial q_i^{(1)}}{\partial x_k}\right)\right]. \tag{48}$$

Eqs. (45) and (46) are similar to the Navier–Stokes–Fourier equations but with extra terms underlined on the right-hand side that account for any rarefaction effects and can be determined from Eqs. (47) and (48). These equations can be expressed in a general conservative form as:

$$\underbrace{\frac{\partial \rho u_k \Phi}{\partial x_k}}_{\text{convective term}} - \underbrace{\frac{\partial}{\partial x_k}\left(\frac{\mu}{\Gamma_\Phi}\frac{\partial \Phi}{\partial x_k}\right)}_{\text{diffusive term}} = \underbrace{S_\Phi}_{\text{source term}}, \tag{49}$$

in which, $\Phi = (u_i, T, g_{ij}, h_i)$, $\Gamma_\Phi = (1, 2/5, 3/2, 5/6)$, and $S_\Phi = (S_{u_i}, S_T, S_{g_{ij}}, S_{h_i})$ corresponds to the right hand terms of Eqs. (45)–(48) respectively. This set of equations is now in a conventional convection-diffusion format with appropriate source terms. The numerical algorithm for solving Eq. (49) has been well documented in many CFD textbooks, such as the one by Ferziger and Perić [36], and has been implemented in a finite volume in-house code, THOR, in the present study. The diffusive and source terms are discretized by a central difference scheme. For the convective terms, a range of upwind schemes including QUICK [37], SMART [38], and CUBISTA [39] are available in THOR and the CUBISTA scheme was selected for the present study. The coupling of the velocity and pressure fields is through the SIMPLE algorithm [40]. A collocated grid arrangement

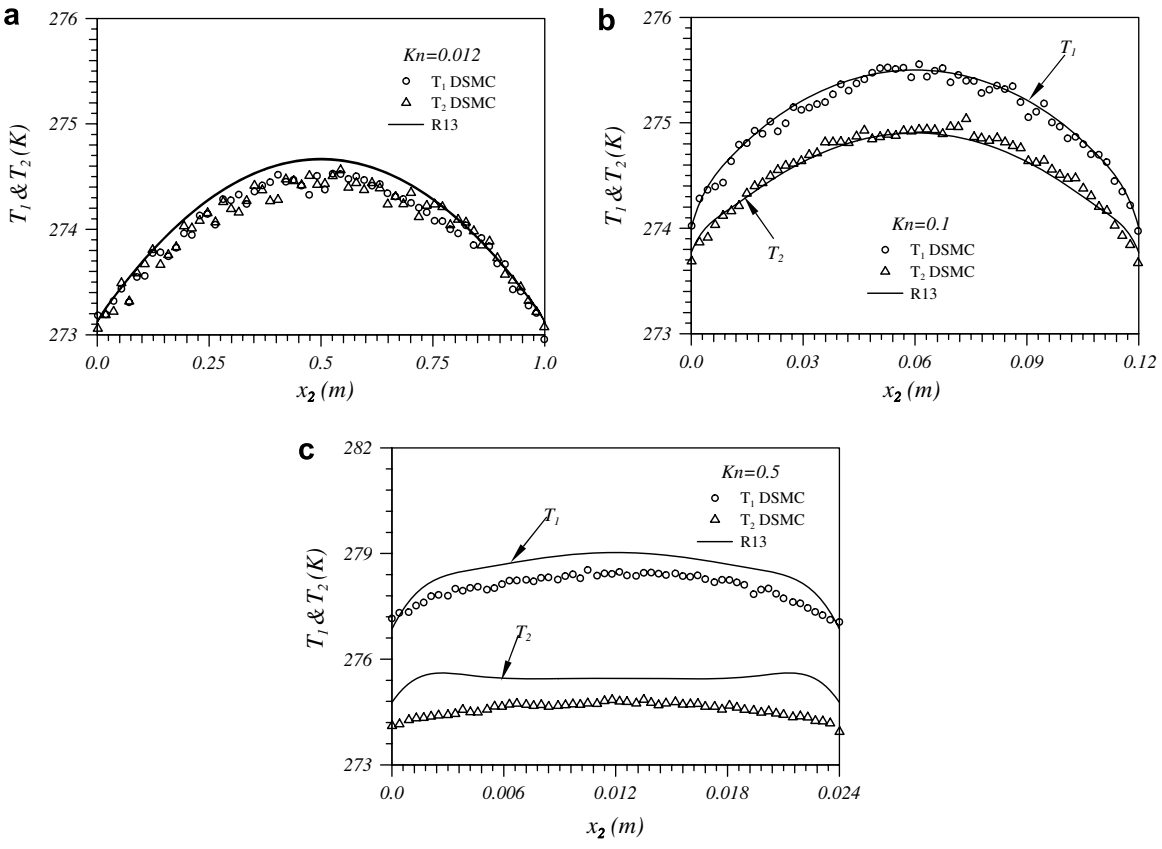

Fig. 5. Computed profiles of temperatures in directions x_1 and x_2 with initial conditions: $T_w = 273$ K and $u_w = 100$ m/s.

is used in THOR and the interpolation scheme of Rhie and Chow [41] is used to eliminate any resultant non-physical pressure oscillations. The system of 13 moment equations is solved iteratively and the solution procedure can be summarized as follows:

1. Calculate u_i at iteration $n+1$ using the values of other variables at the previous iteration n.
2. Solve the pressure correction equation using the SIMPLE algorithm to update p and u_i at iteration $n+1$.
3. Calculate T, g_{ij} and h_i at iteration $n+1$ using updated pressure and velocity fields.
4. Return to step 1 and repeat until residuals of each governing equation reaches a specified convergence criterion.

6. Results and discussion

Figs. 1a–g present the results of β_ϕ from the DSMC simulations for five wall velocities over a range of Knudsen numbers. Due to the stochastic nature of the DSMC method, the data are scattered but generally lie around a particular value, with weak dependency on the Knudsen number studied. Figs. 1a and b show that the correction factors for slip-velocity and temperature jump, β_u and β_T, respectively, are close to unity when $Kn > 0.1$. These particular factors have been the subject of many previous investigations [1,28–31]. In particular, Figs. 1a and b show results obtained from the solution of the linearized Boltzmann equation [1,28,31] which yielded values of 1.1446 and 1.1682 for β_u and β_T, respectively. These values compare well to the DSMC predictions for $Kn = 0.012$ but tend to overpredict at higher Knudsen numbers. In the present approach, this corresponds to retaining just the first terms in Eqs. (29) and (30), and neglecting all the higher moments i.e. previous work essentially used a first-order approximation for the shear stress and heat flux terms

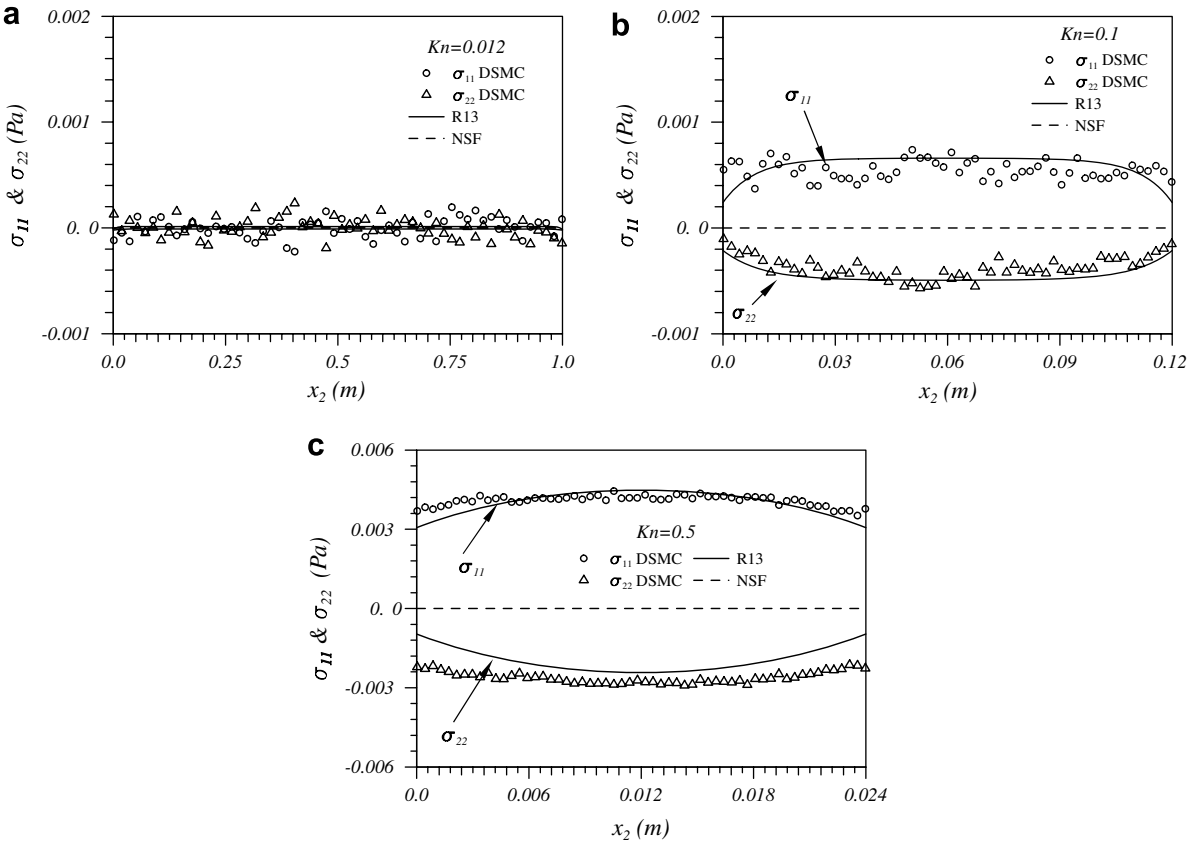

Fig. 6. Computed profiles of normal stresses σ_{11} and σ_{22} with initial conditions: $T_w = 273$ K and $u_w = 100$ m/s.

to derive the values of β_u and β_T. The authors are not aware of any theoretical or numerical values of the correction factors for wall stresses and heat fluxes that contain the higher-order moments.

The solid lines shown in Fig. 1 are the values of β_φ used for the solution of Eqs. (8)–(12) in the present study. The DSMC data has strongly guided the analysis but the coefficients have been further optimized from the solution of the R13 equations for Couette flow. One particular feature of planar Couette flow is having a constant shear stress throughout the domain. Fig. 1e shows that the value of $\beta_{\sigma_{12}}$ required to obtain a constant shear stress, σ_{12}, for the R13 equations is significantly above the value predicted by the DSMC results. The difficulty is clearly highlighted in Fig. 2 which shows how the predicted shear stress varies with different values of $\beta_{\sigma_{12}}$. The reason for the non-constant behavior is due to the occurrence of the term m_{122} in Eqs. (11) and (33). As the Knudsen number increases, this term becomes very nonlinear and is poorly predicted at the wall and its impact will be discussed later. The best fit was for $\beta_{\sigma_{12}} = 1.36$ and a complete list of the values of β_φ used to solve the R13 equations are listed in Table 1.

The DSMC results showed a similar variation with Knudsen number for all values of wall velocity considered in this study. Consequently, only results for $u_w = 100$ m/s will be presented and discussed. The NSF and R13 equations were solved using an in-house finite-volume CFD code, THOR, and the velocity slip and temperature jump boundary conditions for the NSF equations have been taken from Cercignani [1]. For the 1D Couette flow in the present study, 200 equi-spaced grid points have been used in the solution domain, which was sufficient for grid independent solutions to be achieved. The computed values of tangential velocity (u_1) and temperature are presented in Figs. 3 and 4 for $Kn = 0.012$, 0.1 and 0.5, respectively. At $Kn = 0.012$, Figs. 3a and 4a show that both hydrodynamic models give almost identical values for both velocity and temperature. The values of u_1 from the NSF and R13 equations are in very good agreement with the DSMC data but, although the hydrodynamic models give the correct temperature jump, they appear to overpredict the maximum value of temperature. However, there is significant difficulty in reducing the thermal noise associated with the DSMC simulation at such a low Knudsen number. As Kn increases to 0.1, both the R13 and NSF equations start to

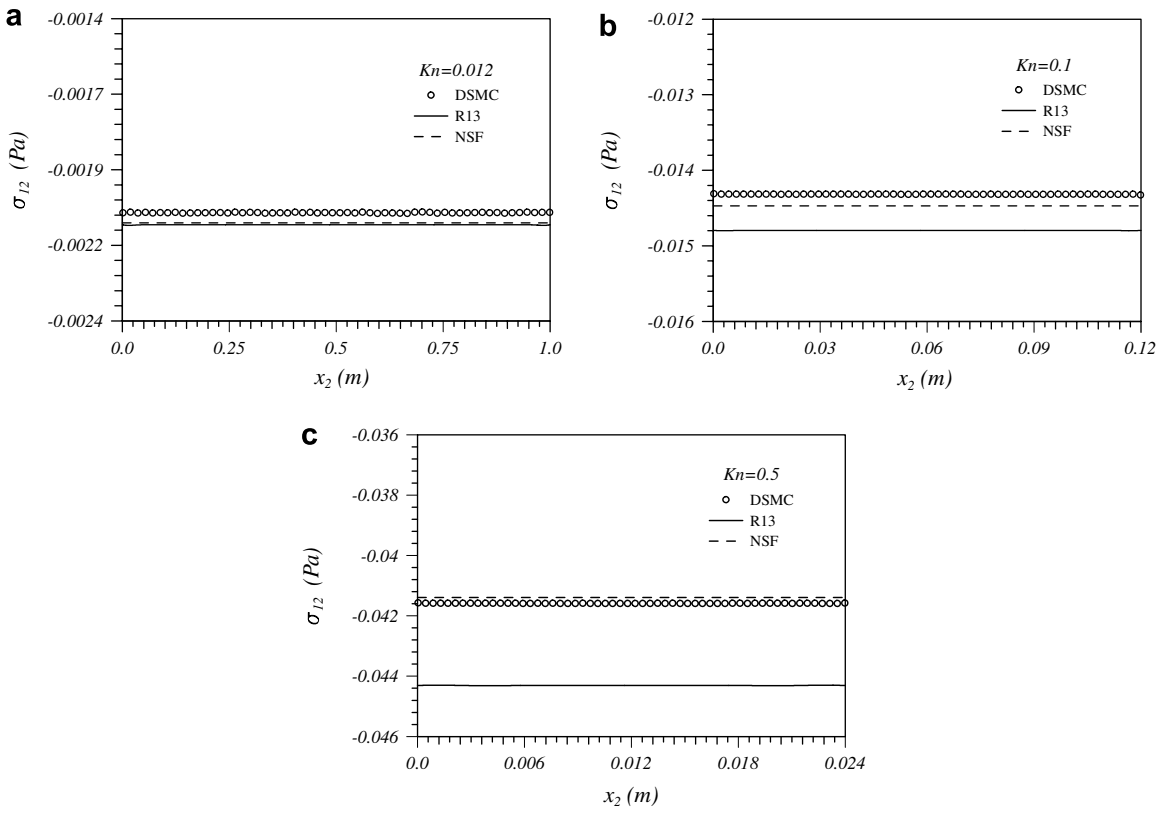

Fig. 7. Computed profiles of shear stress, σ_{12}, with initial conditions: $T_w = 273$ K and $u_w = 100$ m/s.

slightly overpredict the velocity slip. Fig. 3b shows that the predicted values of u_1 from the R13 equations are in better agreement with the DSMC data than the NSF results whereas Fig. 4b indicates that the R13 and NSF equations slightly overpredict the temperature jump. Overall, the values of T from the R13 are in closer agreement with DSMC than those from NSF. At $Kn = 0.5$, well into the transition regime, Figs. 3b and 4b illustrate that the values of u_1 and T from the NSF equations deviates substantially from the DSMC results whilst those from the R13 are in general agreement with the DSMC data apart from near wall region. The overprediction of temperature from the R13 equations at $Kn = 0.5$ can be attributed to the incorrect shear stress.

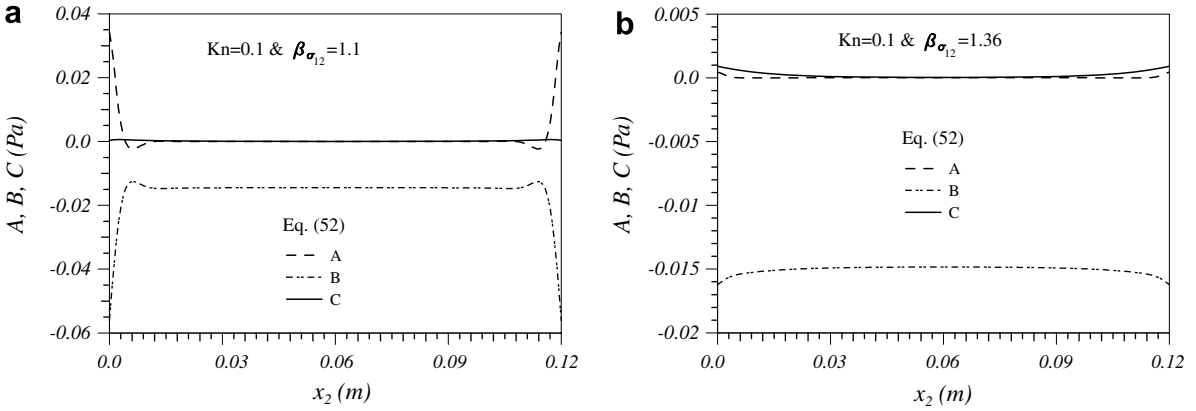

Fig. 8. Budget of the equation of shear stress σ_{12} in Couette flow.

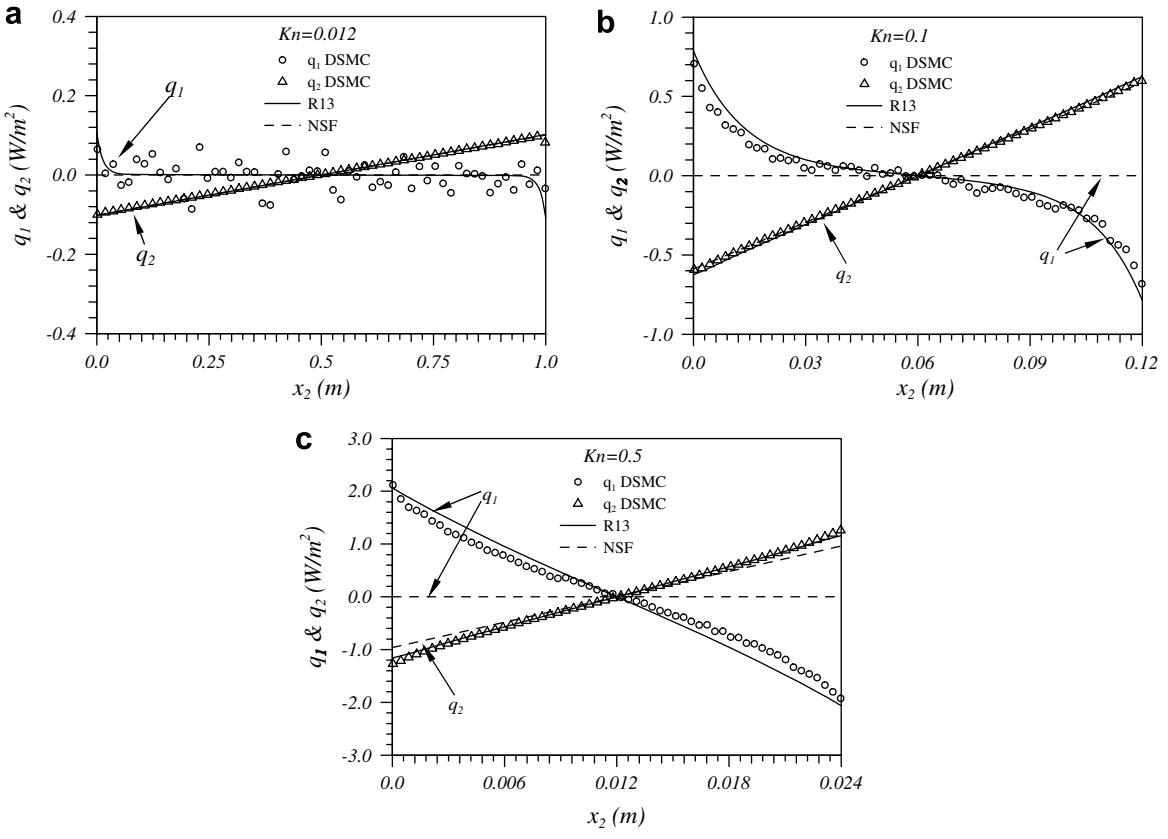

Fig. 9. Profiles of tangential and normal heat fluxes q_1 and q_2 for Couette flow with $T_w = 273$ K and $u_w = 100$ m/s.

The temperature shown in Fig. 4 is defined in Eq. (6), which includes energy components in the three spatial dimensions. A separate temperature field in each individual direction can also be defined [3]. For example, temperatures T_1 and T_2 in the x_1 and x_2 directions, respectively, are defined by

$$\rho\frac{k}{m}T_1 = \int c_1^2 f \,\mathrm{d}\boldsymbol{\xi} \quad \text{and} \quad \rho\frac{k}{m}T_2 = \int c_2^2 f \,\mathrm{d}\boldsymbol{\xi}. \tag{50}$$

From the above definitions, it is straightforward to obtain the following relationships:

$$T_1 = T + \frac{\sigma_{11}}{\rho R} \quad \text{and} \quad T_2 = T + \frac{\sigma_{22}}{\rho R}. \tag{51}$$

The profiles of T_1 and T_2 predicted by the R13 equations are shown in Fig. 5 and compared with the DSMC results for different values of Kn. At $Kn = 0.012$, the computed values of T_1 and T_2, from both the R13 equations and DSMC, are in close agreement. Each temperature field has the same value because the flow is very close to equilibrium and any rarefaction effects are therefore weak. When the value of Kn is greater than 0.1, the temperature in each direction is different, as clearly shown in Figs. 5b and 5c, with $T_1 > T > T_2$ i.e. the temperature parallel to the walls is higher than that perpendicular to the walls. This is because the values of the normal stresses, σ_{11} and σ_{22}, are no longer zero.

Figs. 6 and 7 show the computed values of normal stresses σ_{11} and σ_{22}, and shear stress σ_{12}, from both DSMC and hydrodynamic models for several Knudsen numbers. At $Kn = 0.012$, shown in Fig. 6a, both the R13 and NSF equations produce a value of zero for σ_{11} and σ_{22} whilst those from the DSMC simulation are scattered around a value of zero. Fig. 7a illustrates that the values of σ_{12} computed from the three approaches are also in close agreement. At $Kn = 0.1$ and 0.5, the DSMC results demonstrate that both σ_{11} and σ_{22} are no longer zero. As shown in Figs. 6b and 6c, the R13 equations are able to capture this departure

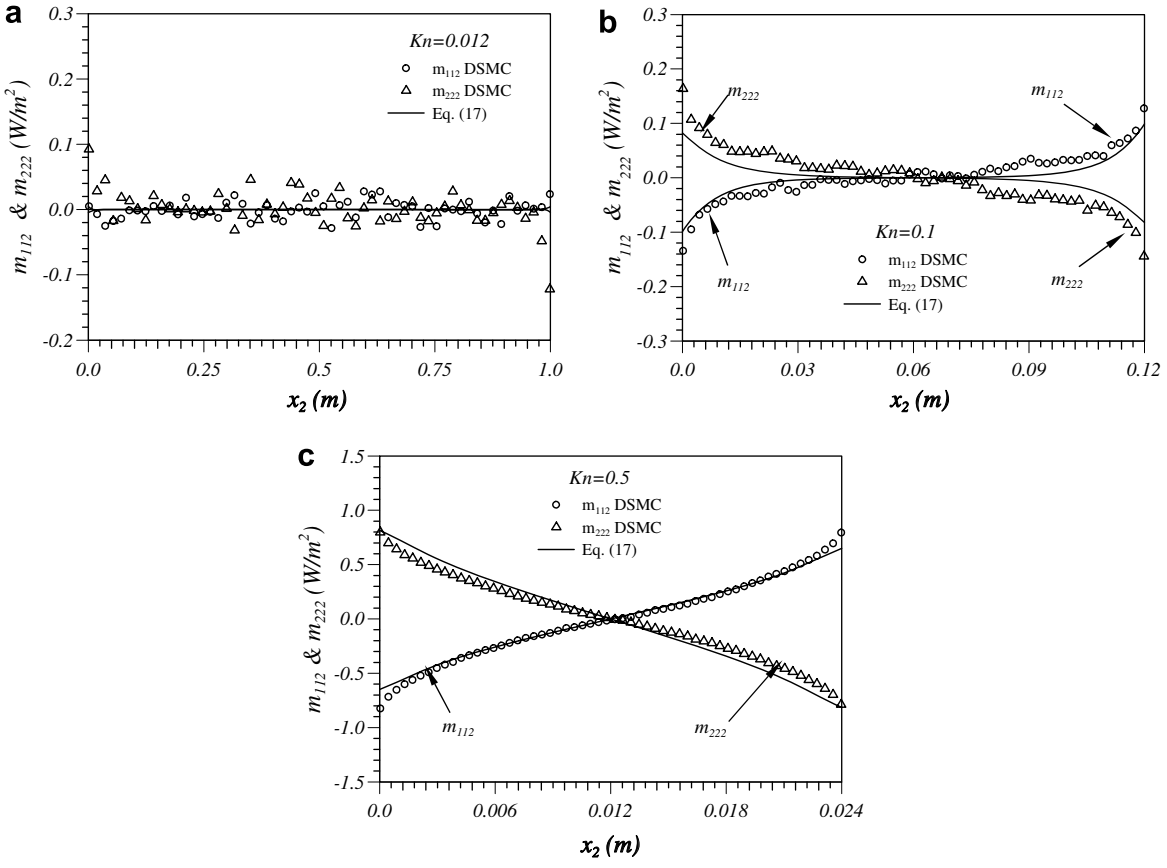

Fig. 10. Profiles m_{112} and m_{222} for Couette flow with $T_w = 273$ K and $u_w = 100$ m/s.

from equilibrium reasonably well, apart from very close to the wall. It is interesting to note that the predicted values of shear stress from the NSF equations are in better agreement with the DSMC data than those from the R13 equations, as shown in Figs. 7b and 7c, but it must be remembered that the values for σ_{12} predicted by the NSF equations are evaluated from incorrect velocity profiles. The poor shear stress prediction has also been observed by Struchtrup [17] who used the superposition approach to obtain values of σ_{12} from the R13 equations.

For planar Couette flow, Eq. (11) for the shear stress can be reduced to

$$\sigma_{12} = \frac{\left[-\frac{\mu}{p}\frac{\partial m_{122}}{\partial x_2}\right]}{A} + \frac{\left[-(p+\sigma_{22})\frac{\mu}{p}\frac{\partial u}{\partial x_2}\right]}{B} + \frac{\left[-\frac{2}{5}\frac{\mu}{p}\frac{\partial q_1}{\partial x_2}\right]}{C}. \tag{52}$$

The values of the terms A, B, and C in Eq. (52) are shown in Fig. 8 for $Kn = 0.1$ with $\beta_{\sigma_{12}} = 1.1$ and $\beta_{\sigma_{12}} = 1.36$, respectively. When $\beta_{\sigma_{12}} = 1.1$, term C is negligible in comparison to the other two terms, whilst A and B change dramatically as the wall is approached but in opposite directions due to the nonlinearity of the velocity profile in the regions near the wall, as indicated by the broken line curve in the enlarged part of Fig. 3b. However, the rate of change of A is lower than for term B, which results in the broken line curve in Fig. 2. To correct this, a value larger than the DSMC results suggest was given to $\beta_{\sigma_{12}}$. This increased the magnitude of the shear stress and slip velocity, but also reduced the nonlinearity of the velocity profile. With $\beta_{\sigma_{12}} = 1.36$, each term in Eq. (52) changes smoothly and results in a uniform value of σ_{12}, as shown in Fig. 2 by the solid line.

An interesting nonequilibrium phenomenon that occurs in planar Couette flow is the appearance of a heat-flux without the presence of a temperature gradient. If the upper and lower walls are held at a fixed

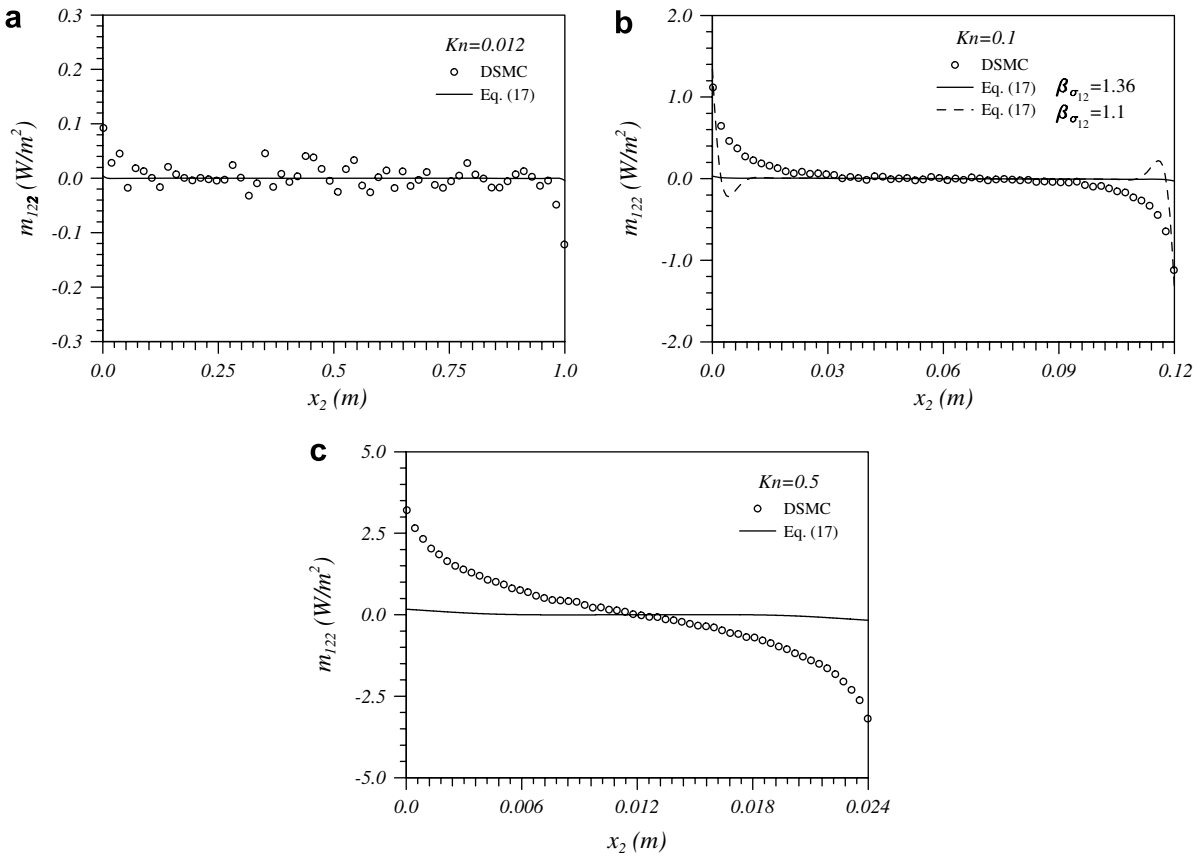

Fig. 11. Profiles of m_{122} for Couette flow with $T_w = 273$ K and $u_w = 100$ m/s.

temperature, T_w, the NSF equations predict that the tangential heat flux, q_1, is zero for any value of Knudsen number. Fig. 9a presents the normal and tangential heat fluxes for $Kn = 0.012$. Statistical scatter is evident in the DSMC data but both continuum approaches show the correct trend, although the R13 equations do predict a small amount of tangential heat flux very close to the wall. At the upper continuum limit ($Kn = 0.1$), a significant amount of tangential heat flux is predicted, as shown in Fig. 9b. This feature is captured quite well by the R13 equations but the NSF equations completely fail to predict this aspect of the flow. At $Kn = 0.5$, Fig. 9c shows that the predicted values of tangential heat flux from the R13 equations still closely follow the DSMC data. In contrast, Figs. 9a and b indicate that the normal heat flux is captured well by both continuum-based schemes up to $Kn = 0.1$. However, beyond this value, Fig. 9c shows that the NSF equations start to underpredict the DSMC data.

The ability of the 13 moment equations to accurately capture stresses at large values of Knudsen number will clearly be affected by the approximation of the moment terms m_{ijk}, R_{ij} and Δ. Grad [7] assumed $m_{ijk} = R_{ij} = \Delta = 0$ whilst Struchtrup [15] derived a first-order approximation. At $Kn = 0.012$, the values of m_{112}, m_{222} and m_{122} are very close to zero, as illustrated in Figs. 10a and 11a. These predictions are supported by the DSMC data which indicates that these third moments are scattered around zero. At this low value of Knudsen number, the contribution of m_{ijk} in Eq. (11) is therefore negligible. However, as the value of Kn starts to increase, the contribution of m_{ijk} becomes progressively more important. Figs. 10b and 10c compare the R13 and DSMC predictions for $Kn = 0.1$ and 0.5, respectively. At the continuum limit, the first-order approximation of m_{ijk} provides a reasonable estimate for both m_{112} and m_{222} and certainly captures the correct trend. Unfortunately, the behavior of m_{122} is not predicted very well, particularly near the wall for either value of $\beta_{\sigma_{12}}$(1.1 or 1.36), as shown in Fig. 11b. As the degree of rarefaction is increased, the weakness of the first-order approximation becomes very apparent. Fig. 10c illustrates that the behaviors of m_{112} and m_{222} are captured quite well in comparison with DSMC results. However, the scale of the problem is clearly reflected in the fact

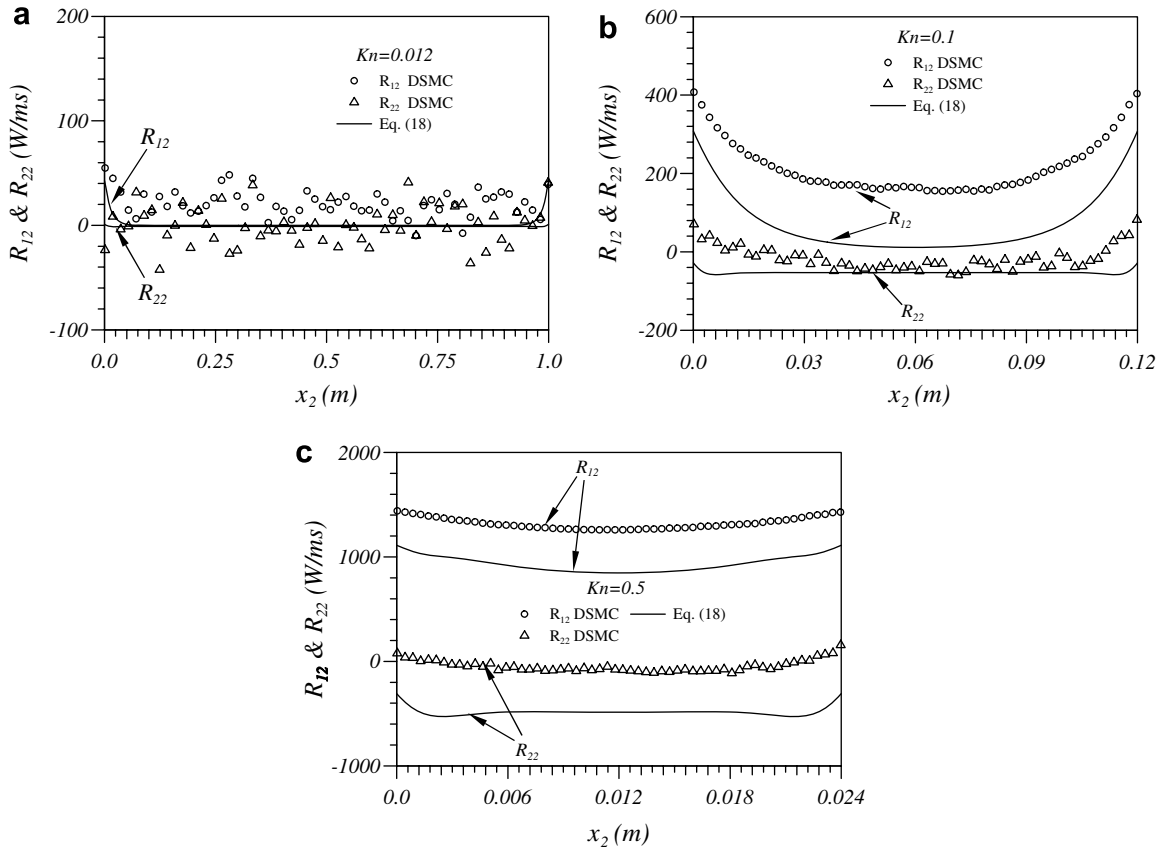

Fig. 12. Profiles of R_{12} and R_{22} for Couette flow with $Kn = 0.5$, $T_w = 273$ K and $u_w = 100$ m/s.

that the m_{122} term consistently predicts a value close to zero. The direct consequence of these results is that the stresses, given in Eq. (11), do not agree with the DSMC data at larger values of the Knudsen number.

Comparisons of the predicted values of R_{12} and R_{22} with DSMC data are shown in Fig. 12 for different values of the Knudsen number. Fig. 12a shows that when $Kn = 0.012$, R_{22} is close to zero, consistent with DSMC data, which is also scattered around zero, but the R13 equations and the DSMC results appear to predict a small but finite value for R_{12}. As the value of the Knudsen number increases to 0.1 and above, Figs. 12b and c indicate that the values of both R_{12} and R_{22} start to depart from zero. Although Eq. (18) generally follows the trend of the DSMC results, the magnitude of both R_{12} and R_{22}, are not predicted particularly well.

The results imply that the first-order approximation of m_{ijk} and R_{ij} significantly improves Grad's original assumption but a higher-order approximation is probably required to more accurately close the 13 moment equations and successfully model flows further from the slip-flow regime.

7. Conclusions

A numerical method for solving the regularized 13 moment equations has been proposed. To enable confined flows to be modeled, a complete set of wall boundary conditions for the 13 moment equations has been derived, based on the Maxwell wall-boundary model and a fourth-order approximation of the molecular distribution function in Hermite polynomials. Empirical correction factors were introduced into the wall boundary conditions to account for Knudsen layer effects and were calibrated with direct simulation Monte Carlo data. Computational results of planar Couette flow over a range of wall velocities and Knudsen numbers showed that the R13 equations recovered the continuum solution at small values of the Knudsen number ($\leqslant 0.012$) and performed much better than the Navier–Stokes–Fourier equations for velocity, temperature, and heat flux at Knudsen numbers above 0.012.

The limitation of a first-order approximation to the third moment, m_{ijk}, was highlighted and this truncation leads directly to the R13 equations predicting a non-constant shear stress as the degree of rarefaction increases. This error was partially accounted for by introducing a coefficient that was higher that the value obtained from direct simulation Monte Carlo data. However, it was also observed that the magnitude of both R_{12} and R_{22}, are not predicted particularly well at higher Knudsen numbers. It is clear that the first-order approximation of m_{ijk} and R_{ij} brings many improvements to Grad's original assumption but a higher-order approximation is probably required for the 13 moment equations to successfully model flows that depart further from the slip-flow regime. Alternatively, a transport equation could be introduced for the m_{ijk} term but this would have the disadvantage of requiring additional wall-boundary conditions.

Acknowledgements

The paper has benefited greatly from discussions with Professor Stefan Stefanov (Bulgarian Academy of Science), Professor Jason Reese (University of Strathclyde), Dr. Yingsong Zheng during his visit to the University of Strathclyde, Drs. Robert Barber and Y. H. Zhang at Daresbury Laboratory. The authors thank the Engineering and Physical Sciences Research Council (EPSRC) for their support of Collaborative Computational Project 12 (CCP12).

Appendix

The expressions of the polynomials and their associated coefficients used in Section 3 to derive the fourth-order approximation of the molecular distribution function, $f^{(4)}$, are [7]:

$$\begin{cases} H^{(0)} = 1, H_i^{(1)} = \dfrac{c_i}{\sqrt{RT}}, H_{ij}^{(2)} = \dfrac{c_i c_j}{RT} - \delta_{ij}, \\ H_{ijk}^{(3)} = \dfrac{c_i c_j c_k}{\left(\sqrt{RT}\right)^3} - \dfrac{c_i\delta_{jk} + c_j\delta_{ik} + c_k\delta_{ij}}{\sqrt{RT}}, \\ H_{ijkl}^{(4)} = \dfrac{c_i c_j c_k c_l}{RT^2} - \dfrac{c_i c_j\delta_{kl} + c_i c_k\delta_{jl} + c_i c_l\delta_{jk} + c_j c_k\delta_{il} + c_j c_l\delta_{ik} + c_k c_l\delta_{ij}}{RT} + \left(\delta_{ij}\delta_{kl} + \delta_{ik}\delta_{jl} + \delta_{il}\delta_{jk}\right) \end{cases} \tag{A.1}$$

and

$$\begin{cases} a^{(0)} = 1, a_i^{(1)} = 0, a_{ij}^{(2)} = \dfrac{\sigma_{ij}}{p}, \\ a_{ijk}^{(3)} = \dfrac{\rho_{ijk}}{p\sqrt{RT}}, \\ a_{ijkl}^{(4)} = \dfrac{\rho_{ijkl}}{pRT} - \dfrac{\sigma_{ij}\delta_{kl} + \sigma_{ik}\delta_{jl} + \sigma_{il}\delta_{jk} + \sigma_{jk}\delta_{il} + \sigma_{ji}\delta_{ik} + \sigma_{kl}\delta_{ij}}{p} - \left(\delta_{ij}\delta_{kl} + \delta_{ik}\delta_{jl} + \delta_{il}\delta_{jk}\right), \end{cases} \tag{A.2}$$

respectively. The trace and traceless parts of the moments are

$$\begin{aligned} \rho_{ijkl} = \rho_{\langle ijkl\rangle} &+ \frac{1}{7}\left(\rho_{\langle ij\rangle rr}\delta_{kl} + \rho_{\langle ik\rangle rr}\delta_{jl} + \rho_{\langle il\rangle rr}\delta_{jk} + \rho_{\langle jk\rangle rr}\delta_{il} + \rho_{\langle jl\rangle rr}\delta_{ik} + \rho_{\langle kl\rangle rr}\delta_{ij}\right) \\ &+ \frac{1}{15}\left(\delta_{ij}\delta_{kl} + \delta_{ik}\delta_{jl} + \delta_{il}\delta_{jk}\right)\rho_{rrss}. \end{aligned} \tag{A.3}$$

$$\rho_{ijk} = \rho_{\langle ijk\rangle} + \frac{2}{5}\left(q_i\delta_{jk} + q_j\delta_{ik} + q_k\delta_{ij}\right). \tag{A.4}$$

Using Eq. (13) and $\rho_{\langle ijkl\rangle} = \phi_{ijkl}$, it can be shown that

$$\begin{cases} a^{(0)}H^{(0)} = 1,\ a_i^{(1)}H_i^{(1)} = 0,\ a_{ij}^{(2)}H_{ij}^{(2)} = \dfrac{\sigma_{ij}c_ic_j}{pRT}, \\ a_{ijk}^{(3)}H_{ijk}^{(3)} = \dfrac{m_{ijk}c_ic_jc_k}{p(RT)^2} + \dfrac{6c^2c_iq_i}{5p(RT)^2} - \dfrac{6c_iq_i}{pRT}, \\ a_{ijkl}^{(4)}H_{ijkl}^{(4)} = \dfrac{\phi_{ijkl}c_ic_jc_kc_l}{p(RT)^3} + \dfrac{6c^2R_{ij}c_ic_j}{7p(RT)^3} - \dfrac{6R_{ij}c_ic_j}{p(RT)^2} - \dfrac{2c^2\Delta}{p(RT)^2} + \dfrac{c^4\Delta}{5p(RT)^3} + \dfrac{3\Delta}{pRT}. \end{cases} \tag{A.5}$$

References

[1] C. Cercignani, Theory and Application of the Boltzmann Equation, Scottish Academic Press, Edinburgh, 1975.
[2] T. Ohwada, Y. Sone, K. Aoki, Numerical analysis of the Poiseuille and thermal transpiration flows between two parallel plates on the basis of the Boltzmann equation for hard sphere molecules, Phys. Fluids A 1 (1989) 2042–2049.
[3] G. Bird, Molecular Gas Dynamics and the Direct Simulation of Gas Flows, Clarendon Press, Oxford, 1994.
[4] J.C. Harley, Y.F. Huang, H.H. Bau, J.N. Zemel, Gas flow in micro-channels, J. Fluids Mech. 284 (1995) 257–274.
[5] M. Gad-el-Hak, The fluid mechanics of microdevices – the freeman scholar lecture, J. Fluids Eng. 121 (1999) 5–33.
[6] S. Chapman, T.G. Cowling, The Mathematical Theory of Non-uniform Gases, Cambridge University Press, Cambridge, 1970.
[7] H. Grad, On the kinetic theory of rarefied gases, Commun. Pure Appl. Math. 2 (1949) 331–407.
[8] H. Grad, Asymptotic theory of the Boltzmann equation, Phys. Fluids 6 (1963) 147–181.
[9] P. Rosenau, Extending hydrodynamics via regularization of Chapman–Enskog solution, Phys. Rev. A 40 (1989) 7193–7196.
[10] X. Zhong, R.W. MacCormack, D.R. Chapman, Stabilization of the Burnett equations and application to hypersonic flows, AIAA J. 31 (1993) 1036–1043.
[11] R.K. Agarwal, K.Y. Yun, R. Balakrishnan, Beyond Navier–Stokes: Burnett equations for flows in the continuum-transition regime, Phys. Fluids 13 (2001) 3061–3085.
[12] H. Grad, The profile of steady plane shock wave, Commun. Pure Appl. Math. 5 (1952) 257–300.
[13] H. Struchtrup, M. Torrilhon, Regularization of Grad's 13 moment equations: Derivation and linear analysis, Phys. Fluids 15 (2003) 2668–2680.
[14] H. Struchtrup, Stable transport equations for rarefied gases at high orders in the Knudsen number, Phys. Fluids 16 (2004) 3921–3934.
[15] H. Struchtrup, Derivation of 13 moment equations for rarefied gas flow to second order accuracy for arbitrary interaction potentials, Multiscale Model. Simul. 3 (2005) 221–243.
[16] S. Jin, M. Slemrod, Regularization of the Burnett equations via relaxation, J. Stat. Phys. 103 (2001) 1009–1033.
[17] H. Struchtrup, Macroscopic Transport Equations for Rarefied Gas Flows, Springer, Berlin Heidelberg, 2005.
[18] M. Torrilhon, H. Struchtrup, Regularized 13 moment equations: Shock structure calculations and comparison to Burnett models, J. Fluid Mech. 513 (2004) 171–198.
[19] C. Cercignani, Rarefied Gas Dynamics: From Basic Concepts to Actual Calculations, Cambridge University Press, Cambridge, 2000.
[20] J.C. Maxwell, On stresses in rarified gases arising from inequalities of temperature, Phil. Trans. Roy. Soc. (Lond.) 170 (1879) 231–256.
[21] H. Versteeg, W. Malalaserkera, An Introduction to Computational Fluid Dynamics, The Finite Volume Method, Pearson Education Ltd., Harlow England, 1995.

[22] E.F. Toro, Riemann Solvers and Numerical Methods for Fluids Dynamics: A Practical Introduction, second ed., Springer, Berlin, 1999.
[23] A. Harten, High-resolution schemes for hyperbolic conservation-laws, J. Comput. Phys. 49 (1983) 357–393.
[24] X.D. Liu, S. Osher, Convex ENO high order multi-dimensional schemes without field by field decomposition or staggered grids, J. Comput. Phys. 142 (1998) 304–330.
[25] S. Jin, L. Pareshi, M. Slemrod, A relaxation scheme for solving the Boltzmann equation based on the Chapman–Enskog expansion, Acta Math. Appl. Sinica 18 (2002) 37–62.
[26] C. Truesdell, R.G. Muncaster, Fundamentals of Maxwell's Kinetic Theory of a Simple Monotomic Gas, Academic Press, New York, 1980.
[27] H. Struchtrup, W. Weiss, Temperature jump and velocity slip in the moment method, Continuum Mech. Thermodyn. 12 (2000) 1–18.
[28] S. Albertoni, C. Cercignani, L. Gotusso, Numerical evaluation of the slip coefficient, Phys. Fluids 6 (1963) 993–996.
[29] S.K. Loyalka, N. Petrellis, T.S. Storvick, Some numerical results for BGK model: thermal creep and viscous slip problems with arbitrary accommodation at the surface, Phys. Fluids 18 (1975) 1094–1099.
[30] F. Sharipov, V. Seleznev, Data on internal rarefied gas flows, J. Phys. Chem. Ref. Data 27 (1998) 657–706.
[31] P. Bassanini, C. Cercignani, C.D. Pagni, Comparison of kinetic theory analyses of linearized heat transfer between parallel plates, Int. J. Heat Mass Transfer 10 (1967) 447.
[32] W. Marques Jr., G.M. Kremer, F.M. Sharipov, Couette flow with slip and jump boundary conditions, Continuum Mech. Thermodyn. 12 (2000) 379–386.
[33] D.A. Lockerby, J.M. Reese, High-resolution Burnett simulations of micro Couette flow and heat transfer, J. Comput. Phys. 188 (2003) 333–347.
[34] H. Xue, H.M. Ji, C. Shu, Analysis of micro-Couette flow using the Burnett equations, Int. J. Heat Mass Transfer 44 (2001) 4139–4146.
[35] F.M. White, Viscous Fluid Flow, McGraw-Hill Inc., New York, 1991.
[36] J.H. Ferziger, M. Perić, Computational Methods for Fluid Dynamics, Second ed., Springer, Berlin Heidelberg, 1999.
[37] B.P. Leonard, A stable and accurate convection modelling procedure based on quadratic upstream interpolation, Comput. Mech. Appl. Mech. Eng. 19 (1979) 59–98.
[38] P.H. Gaskell, A.K.C. Lau, Curvature-compensated convective-transport – SMART, A new boundedness-preserving transport algorithm, Int. J. Numer. Meth. Fluids 8 (1988) 617–641.
[39] M.A. Alves, P.J. Oliveira, F.T. Pinho, A convergent and universally bounded interpolation scheme for the treatment of advection, Int. J. Numer. Meth. Fluids 41 (2003) 47–75.
[40] S.V. Patankar, Numerical Heat Transfer and Fluid Flow, McGraw-Hill, New York, 1980.
[41] C.M. Rhie, W.L. Chow, Numerical study of turbulent flow past an airfoil with trailing edge separation, AIAA J. 21 (1983) 1525–1532.